Monthly Notices of the ROYAL ASTRONOMICAL SOCIETY

MNRAS **00,** 1–14 (2024)
Advance Access publication 2024 November 28

https://doi.org/10.1093/mnras/stae2616

NGTS-31b and NGTS-32b: two inflated hot jupiters orbiting subgiant stars

Jose I. Vines [1★] James S. Jenkins,[2,3] David R. Anderson,[1] Douglas R. Alves [4] Maximiliano Moyano,[1] Jack S. Acton,[5] Ioannis Apergis [6,7] Khalid Barkaoui [8,9,10] Daniel Bayliss [11,12] Francois Bouchy,[13] Edward M. Bryant [14] Matthew R. Burleigh,[5] Sarah L. Casewell [5] Jessie L. Christiansen,[15] Karen A. Collins,[7] Philipp Eigmüller,[16] Ben Falk,[17] Samuel Gill,[6,7] Edward Gillen [18] Michael R. Goad,[5] Maximilian N. Günther [19] Beth A. Henderson,[5] Alicia Kendall,[5] Monika Lendl [13] James McCormac,[11,12] Louise D. Nielsen,[20] Ares Osborn [11,12] Gavin Ramsay [21] George R. Ricker,[10] Pamela Rowden [9] Alexander Rudat,[10] Suman Saha,[2,3] Sara Seager,[9,22] Alexis M. S. Smith [16] Thiam-Guan Tan,[8] Rosanna H. Tilbrook [5] Stéphane Udry,[6] Richard West [11] Peter J. Wheatley [11,12] Joshua N. Winn[23] and Tafadzwa Zivave[6,7]

Affiliations are listed at the end of the paper

Accepted 2024 November 4. Received 2024 November 3; in original form 2024 February 7

ABSTRACT

We present the discoveries of NGTS-31b(= TOI-2721), and NGTS-32b, two hot Jupiters from the Next Generation Transit Survey (NGTS) transiting slightly evolved stars. The orbital periods, radii, and masses are 4.16 and 3.31 d, 1.61 and 1.42 R_J, and 1.12 and 0.57 M_J, respectively. Both planets have an incident stellar flux significantly above the threshold where inflation occurs, with both planets showing signs of inflation. These planets have widely different equilibrium temperatures than other hot Jupiters of similar mass and radius, with NGTS-31b having a significantly lower temperature, and NGTS-32b being hotter. This dichotomy raises the question of how prevalent the roles of other inflation mechanisms are in the radius anomaly phenomena and will help further constrain different inflationary models.

Key words: techniques: photometric – planetary systems.

1 INTRODUCTION

The mixture of both radial-velocity (RV) and photometric surveys have allowed us to characterize a wealth of different types of exoplanets fully; from the exotic hot Jupiters (HJs; Charbonneau et al. 2000; Henry et al. 2000; Bayliss et al. 2018), Jupiter-sized planets with orbits shorter than ten days; the ultra-short period planets that have extremely fast orbits with periods of less than one day (USPs; Queloz et al. 2009; Vines et al. 2019; McCormac et al. 2020); and the rare Neptunes (West et al. 2019; Jenkins et al. 2020) in the Neptune-desert, a dearth of Neptune-sized planets with periods shorter than 2−4 d (Helled, Lozovsky & Zucker 2016). While HJs are apparently rare, with around 1 per cent of Sun-like stars hosting them (Wright et al. 2012; Zhou et al. 2019), they are relatively easy to find and confirm due to their high masses and radii (which makes RV signatures and transits easier to detect), and their short orbital periods, which also increases the transit probability.

Having such short periods, HJs are subject to high levels of incident flux, leading to extreme formation and evolution scenarios. It was theorized that thanks to their high incident flux, HJs would be less efficient at cooling than their cooler counterparts, and as a result, they would have larger radii at a given age (Guillot et al. 1992). The hundreds of HJs discovered to date have shown us that their radii are generally significantly larger than theoretical structure models (e.g. Anderson et al. 2011; Tilbrook et al. 2021; Alves et al. 2022). This phenomenon is known as the radius anomaly, and understanding it has become an important objective within the exoplanet community (see Fortney, Dawson & Komacek 2021 and references therein).

Multiple mechanisms have been proposed to explain the radius anomaly, such as HJs having an increased atmospheric opacity (Burrows et al. 2007), having double-diffusive layered convection interiors (Kurokawa & Inutsuka 2015), or energy supplied by the tidal dissipation inside a planet, which also leads to the orbital circularization of HJs (Bodenheimer, Lin & Mardling 2001; Leconte et al. 2010). Other proposed mechanisms exist, and we invite the reader to see Fortney et al. (2021) for a comprehensive review. While there might be multiple effects at play (Sarkis et al. 2021), there is one strong correlation that seems to hold true: incident stellar flux (Weiss et al. 2013; Thorngren & Fortney 2018).

Subgiant stars additionally offer a different set of physical processes that are absent in main-sequence stars, such as the effects of stellar mass-loss on the orbital evolution of these systems or the atmospheric expansion of these stars. Indeed, Lopez & Fortney (2016) predicted that warm Jupiters (e.g. Jupiter-mass planets with equilibrium temperatures lower than 1000 K) would ‘reinflate’ as

★ E-mail: jose.vines.l@gmail.com

Table 1. NGTS photometry for NGTS-31 and NGTS-32. The full table is available in a machine-readable format from the online journal. A portion is shown here for guidance.

Time (BJD-2450000)	Flux (normalized)	Flux error	Star
8789.67778568	0.98734	0.01283	NGTS-31
8789.67793615	0.98456	0.01283	NGTS-31
8789.67808661	0.99887	0.01286	NGTS-31
⋮	⋮	⋮	⋮
8529.79366748	1.00669	0.01286	NGTS-32
8529.79381794	1.01147	0.01286	NGTS-32
8529.79396840	0.98087	0.01280	NGTS-32
⋮	⋮	⋮	⋮

their host stars evolved off of the main sequence and their equilibrium temperatures rose over 1000 K.

There have been significant efforts in creating statistical and physical models and studies in recent years that aim to characterize the underlying relationship between radius inflation, incident flux, and other proposed mechanisms (e.g. Baraffe, Chabrier & Barman 2008; Thorngren et al. 2016; Sestovic, Demory & Queloz 2018; Komacek et al. 2020; Sarkis et al. 2021) and thus adding HJs with fully characterized orbits to the sample is valuable in stressing and testing these models.

In this paper, we report the discovery of two new inflated HJ planets from the Next Generation Transit Survey (NGTS; Wheatley et al. 2018). In Section 2, we describe the observations performed both from NGTS and TESS, and ground-based follow-up photometry and spectroscopy. In Section 3, we detail the determination of the stellar parameters from both spectral analysis and spectral energy distribution (SED) fitting, and the methodology used to model the photometric and spectroscopic data to determine the nature of the planets. In Section 4, we further explore the inflated nature of the planets and how they compare against models and the general HJ population. Finally, in Section 5 we lay out our concluding remarks.

2 OBSERVATIONS

2.1 NGTS photometry

Both NGTS-31 and NGTS-32 were observed as part of the NGTS survey. NGTS-31 was observed starting on 2019 November 2, up until 2020 March 22, while NGTS-32 was first observed by NGTS starting 2019 February 15 until 2019 September 20. A total of 163 962 and 177 102 images were obtained for each star, respectively.

The NGTS procedure is described in Wheatley et al. (2018), to summarize, aperture photometry extraction of observations was performed using the `CASUTools`[1] photometry package, after which they were detrended using an adapted version of the SysRem algorithm (Tamuz, Mazeh & Zucker 2005). Initial assessment of the light curves was performed using `ORION`, a modified box-fitting least squares (BLS) algorithm (Kovács, Zucker & Mazeh 2002; Collier Cameron et al. 2006). For NGTS-31, `ORION` identified a period of 4.16 days, while for NGTS-32 the initial period estimate was 3.31 days. In Table 1, we present the unbinned photometry data from NGTS.

[1] http://casu.ast.cam.ac.uk/surveys-projects/software-release

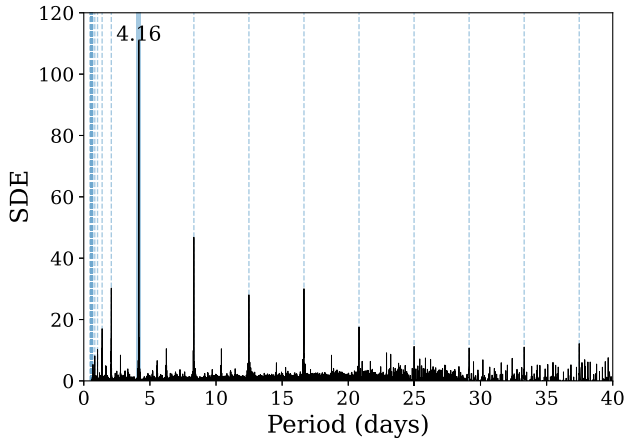

Figure 1. The TLS periodogram analysis of the NGTS-31 *TESS* light curve. Shown in a solid line is the detected transit period of 4.16 days and the dashed lines show the corresponding aliases.

2.2 *TESS* photometry

NGTS-31 was also observed by *TESS* (Ricker et al. 2014) in Sectors 5, 6, 32, and 33 obtaining 30 and 10-min cadence Full Frame Images (FFIs) starting 2018 November 15, and finishing on 2021 January 13. The FFIs were processed with the Quick-Look Pipeline and made publicly available as a High-Level Science Product on MAST (Huang et al. 2020). It was identified as a CTOI by Olmschenk et al. (2021), after which the star was promoted to TOI status as TOI-2721. NGTS-32, on the other hand, has not been observed by *TESS* due to it being within one degree of the ecliptic plane.

We independently searched the *TESS* light curve for transits using the `Transit Least Squares`[2] (TLS) `Python` package by Hippke & Heller (2019), and found a period of 4.16 d, consistent with the period found by `ORION` using the NGTS data, with a signal detection efficiency (SDE; Pope, Parviainen & Aigrain 2016) of 111 with no other significant signal detected. We show the TLS periodogram in Fig. 1.

Using Gaia DR3 (Gaia Collaboration 2023), `eleanor`[3] (Feinstein et al. 2019), and `TESSCut` (Brasseur et al. 2019), we searched for possible contaminants that could fall inside the *TESS* aperture and found no contaminating stars in the *TESS* aperture, and thus, expect the light curves to be unaffected by contamination.

2.3 SAAO photometry

Ground-based follow-up for NGTS-32 was taken using the Sutherland High-speed Optical Cameras (SHOC; Coppejans et al. 2013), specifically the 'SHOC'n'disbelief' camera, mounted on the South African Astronomical Observatory's (SAAO) 1-m telescope. Owing to the size of the field of view ($2.85' \times 2.85'$), we were able to select four nearby comparison stars, each fainter than the target. We obtained two partial transits in the same week in May 2024: an egress using 15s exposures on the 8th May and an ingress using 30s exposures on the 11th May, both in *i*' band to easily recover the transit. Unfortunately, the out-of-transit data from the 8th May had to be truncated due to technical issues, after which airmass had

[2] https://github.com/hippke/tls
[3] https://adina.feinste.in/eleanor/

Table 2. Ground based photometric follow-up of NGTS-31. The full table is available in a machine-readable format from the online journal. A portion is shown here for guidance.

Instrument	BJD (−2450000)	Flux (normalized)	Flux error
MEarth	9513.5855	1.0112	0.0050
MEarth	9513.5856	1.0039	0.0047
⋮	⋮	⋮	⋮
PEST	9526.1290	1.0135	0.0065
PEST	9526.1304	1.0066	0.0061
⋮	⋮	⋮	⋮
LCO	9563.554	0.995	0.001
LCO	9563.558	1.000	0.001
⋮	⋮	⋮	⋮

increased significantly once remedied. Through the local python-based SAAO SHOC pipeline, which involves PYRAF (Science Software Branch at STScI 2012), each light curve was bias and flat-field corrected as an initial step. We used the Starlink package autophotom (Eaton et al. 2014) to perform aperture photometry on all 5 stars, choosing aperture sizes to generate a maximum signal-to-noise ratio for each observation, 4 pixels and 6 pixels for the respective nights, where the pixel scale is 0.167 arcsecs per pixel. Background annuli were set to allow for changes in the apparent measured fluxes of the stars, as seeing changes over the night for example. We performed differential photometry on the raw light curves, and the resulting light curves for each night were normalized using order 1 polynomials fitted to the out-of-transit data prior to inclusion in the joint fit.

2.4 Ground based follow-up

We obtained follow-up transits for NGTS-31b with the MEarth-South (Irwin et al. 2015), at Cerro Tololo Inter American Observatory (CTIO) on the 26th of October 2021. Five telescopes were used with the RG715 filter taking a total of 1498 images. To prevent the telescopes from striking their piers, MEarth's German equatorial mounts had to flip to the other side of their piers, or 'meridian flip', during the observation sequence. As that action tends to introduce an offset in the light curve, we discarded 323 images taken after the star had passed through the meridian and, fortunately, after the transit had ended. We noticed a significant linear trend in the data that was detrended during the joint modelling (see Section 3.2).

An additional full transit was observed by the Perth Exoplanet Survey Telescope (PEST)[4] on the 7th of November 2021. PEST is located near Perth, Australia. The 0.3 m telescope is equipped with a 5544 × 3694 QHY183M camera with a gp filter. Images are binned 2 × 2 in software giving an image scale of 0.″7 pixel^{-1} resulting in a 32′ × 21′ field of view. A custom pipeline based on `C-Munipack`[5] was used to calibrate the images and extract the differential photometry.

Finally, a full transit was acquired on the 15th of December 2021 from the Las Cumbres Observatory Global Telescope (LCOGT; Brown et al. 2013) 0.4 m network node at Cerro Tololo Inter-American Observatory in Chile (CTIO) using the Sloan g' filter band. The telescopes are equipped with 2048 × 3072 SBIG STX6303 cameras having an image scale of 0.″57 pixel^{-1} resulting in a 19′ × 29′ field of view. The images were calibrated using the standard LCOGT BANZAI pipeline (McCully et al. 2018) and differential photometric data were extracted using `AstroImageJ` (Collins et al. 2017). The light curves are shown in Fig. 5 and the data are presented in Table 2.

[4] http://pestobservatory.com/
[5] http://c-munipack.sourceforge.net

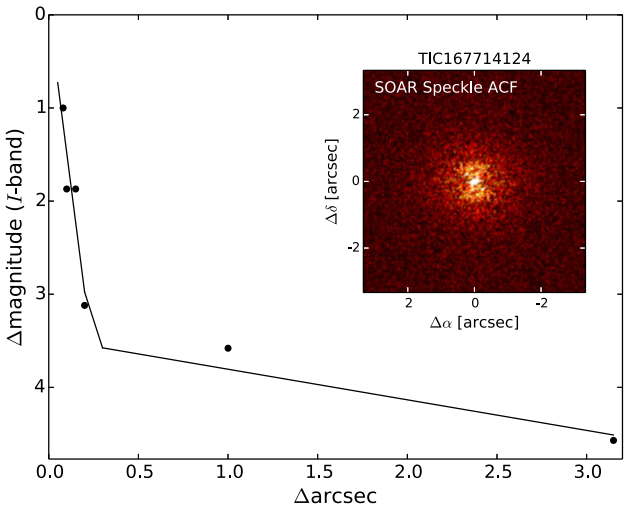

Figure 2. Speckle imaging of NGTS-31 by HRCam at the Southern Astrophysical Research telescope. The contrast curve plots show the linear fit to the 5σ contrast curves on either side of 0.″2. The autocorrelation functions are shown inset.

2.5 SOAR speckle imaging

On 2021 October 1, the 4.1-m SOAR acquired a high-resolution image of NGTS-31 using the HRCam instrument. NGTS-31 (TOI-2721) was observed as part of the SOAR TESS survey (Ziegler et al. 2020, 2021). The contrast curve in the I band and autocorrelation functions can be seen in Fig. 2, where no sign of a companion can be found.

2.6 Spectroscopy

We obtained multi-epoch spectroscopy for both NGTS-31 and NGTS-32 with the FEROS spectrograph, mounted on the 2.2-m MPG/ESO telescope at La Silla observatory (Kaufer et al. 1999), to determine the planetary nature of the transit signals observed in the photometry.

A total of 12 and 20, 20-min observations were performed for NGTS-31 and NGTS-32, respectively, under programs 0108.A-9007(A), 0109.A-9024(A), 0110.A-9035(A), 0111.A-9018(A) (PI: Vines), and 0111.A-9019(A) (PI: Moyano). The observations were carried out with the simultaneous calibration mode with a ThAr + Ne lamp and reduced with the `CERES` pipeline (Brahm, Jordán & Espinoza 2017), which also calculates the RVs using the cross-correlation function (CCF) method. We used a G2 mask and reached an average SNR of 26 and 25 for NGTS-31 and NGTS-32, respectively. The observed RVs can be found in Table 3 and we show the phase folded RVs in Figs 5 and 6.

Table 3. Radial velocities. The full table is available in a machine-readable format from the online journal. A portion is shown here for guidance.

Star	BJD (−2450000)	RV ($m\,s^{-1}$)	ΔRV ($m\,s^{-1}$)
NGTS-31	9493.747	20178.9	15.5
NGTS-31	9501.782	20055.9	11.1
NGTS-31	9502.796	20053.4	12.2
⋮	⋮	⋮	⋮
NGTS-32	9645.670	−79359.3	19.9
NGTS-32	9651.654	−79484.3	22.9
NGTS-32	9656.895	−79289.2	16.3
⋮	⋮	⋮	⋮

Table 4. Four key stellar parameters derived for NGTS-31b and NGTS-32b made using the `SPECIES` code.

Property	Value	Error
NGTS-31		
Teff (K)	5760	120
log g	4.41	0.21
[Fe/H]	0.00	0.05
$v \sin i$ ($km\,s^{-1}$)	6.05	0.63
NGTS-32		
$T_{\rm eff}$ (K)	5790	130
log g	4.10	0.25
[Fe/H]	−0.02	0.05
$v \sin i$ ($km\,s^{-1}$)	6.62	0.56

3 ANALYSIS

3.1 Stellar properties

3.1.1 SPECIES

We analyzed the 1D stacked FEROS spectra using `SPECIES` (Soto & Jenkins 2018; Soto, Jones & Jenkins 2021), an automated code to derive stellar parameters using high-resolution echelle spectra. It makes use of equivalent widths from a number of neutral and ionized iron lines (measured using line equivalent widths, Soto et al. 2021) to derive the atmospheric parameters (temperature, metallicity, surface gravity, and microturbulence). Together with ATLAS9 model atmospheres (Castelli & Kurucz 2004), it solves the radiative transfer and hydrostatic equilibrium equations using MOOG (Sneden 1973), imposing local thermodynamic equilibrium (LTE) conditions, as well as excitation and ionization equilibrium. The rotational and macro turbulent velocities were derived using spectral line fitting and analytic relations, respectively. We summarize `SPECIES` outputs in Table 4.

3.1.2 ARIADNE

Using the outputs from `SPECIES` as priors, we studied the spectral energy distribution (SED) of each star using `ARIADNE`[6], a PYTHON package written to fit SEDs with different stellar atmosphere model grids, which have been previously convolved with several publicly available broad-band filters, in a Bayesian framework (Vines & Jenkins 2022). In order to sample the parameter space, `ARIADNE` utilizes the nested sampling (NS) algorithm implemented in `dynesty`, which calculates the evidence of each model along with the posterior distributions (Skilling 2004, 2006; Higson et al. 2019; Speagle 2020).

`ARIADNE` computes the effective temperature, log g, [Fe/H], Av, and radius of the star using the *Gaia* eDR3 distances from Bailer-Jones et al. (2021), and the line-of-sight V-band extinction found in the SFD dustmap (Schlegel, Finkbeiner & Marc 1998; Schlafly & Finkbeiner 2011) as priors. The final set of parameters is derived through Bayesian model averaging, a weighted average that takes the evidence of each model as weights.

Both NGTS-31 and NGTS-32 were modelled with four atmosphere grids, Phoenix V2 (Husser et al. 2013), BT-Settl (Hauschildt, Allard & Baron 1999; Allard, Homeier & Freytag 2012), Castelli & Kurucz (2004) and Kurucz (1993). In Fig. 3 we show the SEDs for NGTS-31 and NGTS-32 and in Table 5 we report the relevant observational and derived properties along with the method used.

3.1.3 Evolved stars

Our stellar analysis shows that NGTS-31 and NGTS-32 radii are $1.70^{+0.20}_{-0.21}$ and $1.85^{+0.06}_{-0.05}$ $R_\odot$, and ages 9.97 ± 2.58 and $8.03^{+1.03}_{-1.00}$ Gyr, respectively. Along with the derived vsini of each star (6.1 ± 0.6 $km\,s^{-1}$ for NGTS-31 and 6.6 ± 0.6 $km\,s^{-1}$ for NGTS-32), we infer these stars must be evolved. Indeed, when placing these stars in the HR diagram (Fig. 4), we see that both stars are leaving the main sequence and joining the sub-giant branch.

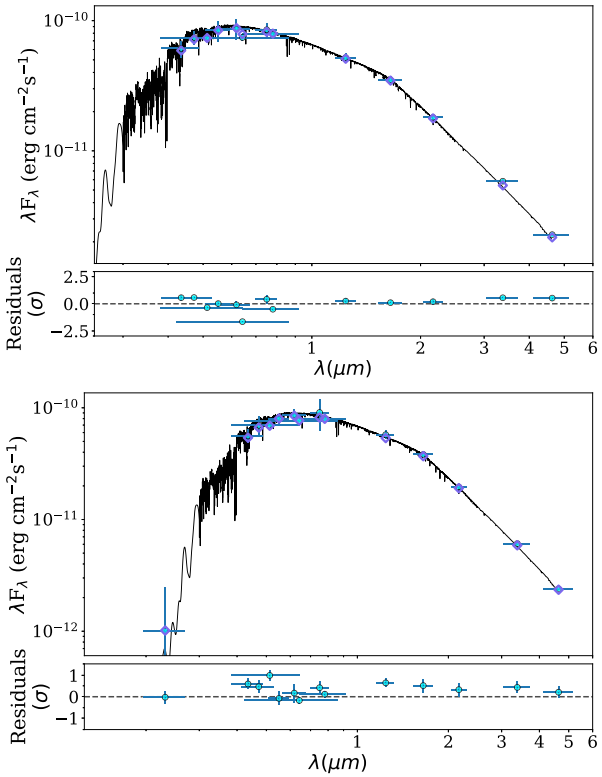

Figure 3. The best-fitting SEDs (black line) for NGTS-31 (top) and NGTS-32 (bottom) based on the photometric data (points) presented in Table 5 are shown in the top panels of both plots. Horizontal error bars show the bandpass width. The diamonds show the synthetic magnitudes at the wavelengths of the photometric data. The lower panels show the residuals to the best-fitting models.

[6] https://github.com/jvines/astroARIADNE

Table 5. Stellar properties.

Property	Value NGTS-31	NGTS-32	Source
2MASS I.D.	05214111–3839245	14552584–1825563	2MASS
Gaia source I.D.	4 819 647 205 326 045 824	6 305 395 724 382 388 224	*Gaia DR3*
TIC I.D.	TIC-167714124	TIC-309694541	TIC8
TOI	2721	-	
Astrometric Properties			
RA	$05^{h}21^{m}41\overset{s}{.}11$	$14^{h}55^{m}25\overset{s}{.}84$	2MASS
Dec.	$-38°39'24\overset{''}{.}51$	$-18°25'56\overset{''}{.}30$	2MASS
$\mu_{\mathrm{R.A.}}$ (mas y^{-1})	-7.5 ± 1.4	-24.8 ± 1.2	UCAC4
$\mu_{\mathrm{Dec.}}$ (mas y^{-1})	-7.5 ± 1.4	-2.4 ± 1.3	UCAC4
Photometric properties			
V (mag)	13.439 ± 0.026	13.497 ± 0.018	APASS
B (mag)	14.118 ± 0.017	14.214 ± 0.016	APASS
g (mag)	13.732 ± 0.011	13.801 ± 0.030	APASS
r (mag)	13.269 ± 0.035	13.279 ± 0.034	APASS
i (mag)	13.079 ± 0.037	13.011 ± 0.077	APASS
G (mag)	13.336 ± 0.003	13.300 ± 0.003	*Gaia*
BP (mag)	13.630 ± 0.003	13.679 ± 0.003	*Gaia*
RP (mag)	12.772 ± 0.004	12.753 ± 0.004	*Gaia*
NGTS (mag)	12.85	12.82	This work
TESS (mag)	12.848 ± 0.006	-	TIC8
J (mag)	12.175 ± 0.023	12.070 ± 0.022	2MASS
H (mag)	11.822 ± 0.024	11.727 ± 0.022	2MASS
Ks (mag)	11.775 ± 0.024	11.689 ± 0.026	2MASS
$W1$ (mag)	11.695 ± 0.023	11.651 ± 0.023	WISE
$W2$ (mag)	11.738 ± 0.020	11.681 ± 0.023	WISE
Derived properties			
T_{eff} (K)	5710 ± 70	5680 ± 60	ARIADNE
$[Fe/H]$	0.00 ± 0.04	-0.03 ± 0.04	ARIADNE
$v \sin i$ (km s^{-1})	6.1 ± 0.6	6.6 ± 0.6	SPECIES
$\log g$	$4.43^{+0.14}_{-0.16}$	4.09 ± 0.21	ARIADNE
M_s(M$_\odot$)	$0.96^{+0.11}_{-0.05}$	$1.07^{+0.06}_{-0.04}$	ARIADNE
$R_s(R_\odot)$	$1.70^{+0.20}_{-0.21}$	$1.85^{+0.06}_{-0.05}$	ARIADNE
ρ (g cm^{-3})	$0.585^{+0.021}_{-0.018}$	$0.253^{+0.016}_{-0.14}$	EMPEROR.T
Age (Gyr)	9.97 ± 2.58	$8.03^{+1.03}_{-1.00}$	ARIADNE
Distance (pc)	852^{+99}_{-100}	846^{+10}_{-7}	ARIADNE
A_{V} (mag)	0.05 ± 0.02	$0.21^{+0.03}_{-0.05}$	ARIADNE

2MASS (Skrutskie et al. 2006); UCAC4 (Zacharias et al. 2013); APASS (Henden & Munari 2014); WISE (Wright et al. 2010); *Gaia* (Gaia Collaboration 2023).

3.1.4 Activity indicators

We studied the activity indices derived using our `CERES-Plusplus` code, an extension to `CERES` that uses its output to compute indicators for the S-index following the procedure of Vaughan, Preston & Wilson (1978), Noyes et al. (1984), and Jenkins et al. (2006); the H $_\alpha$ following the definitions by Kürster et al. (2003) and Gomes da Silva et al. (2011), the Na I D index defined by Díaz, Cincunegui & Mauas 2007; and finally, the He I line as described by Boisse et al. (2009). The CCF FWHM, Inverse Bisector Slope (Toner & Gray 1988; Gray & Baliunas 1995; Queloz et al. 2001), and contrast are extracted from the headers produced by `CERES`. In particular, we analysed the S-index, FWHM, and the BIS and looked for correlations with the RV data for each star using the Pearson r correlation index and by fitting a linear model (of the form $y = mx + n$) to the data (Figs A1 and A2). The results are summarized in Table 6, where the value in parentheses corresponds to the p-value of said correlation index in the case of the person r index. The person r reveals no significant correlation for both stars and the inclination of each linear model is equally conclusive to no significant correlation. Finally, we studied the Generalized Lomb Scargle (GLS; Lomb 1976; Jeffrey 1982; Zechmeister & Kürster 2009) and found no significant signals in any of the activity indices (Figs A4 and A3).

3.2 Global modelling

Prior to modelling, we binned the NGTS data into one-minute bins to decrease the computational cost of modelling. The modelling itself was performed using `EMPEROR.T`, an upgraded version of `EMPEROR` (Pena & Jenkins, in preparation) that can model both light curves and RVs either separately or in a joint model.

`EMPEROR.T` utilizes the Mandel & Agol (2002) quadratic limb-darkening law implemented in the `PyTransit Python` package (Parviainen 2015) with limb-darkening parameters following the parametrization proposed by Kipping (2016) to model the light curves. We also included a dilution and offset to the light curve

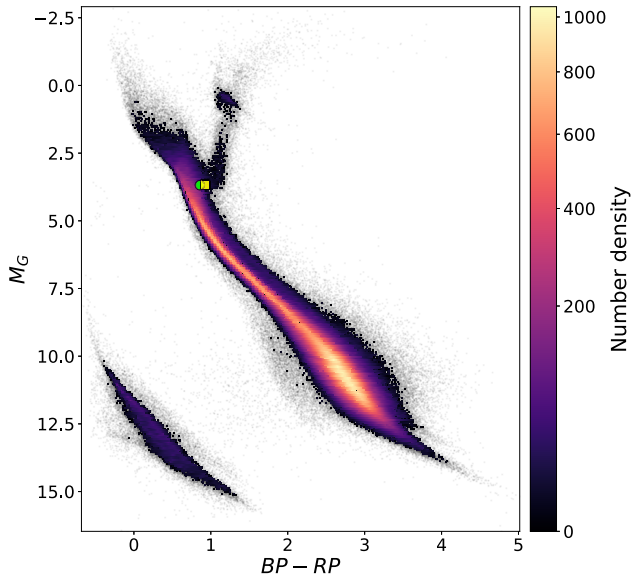

Figure 4. HR diagram constructed from *Gaia*. The green hexagon is NGTS-31 and the yellow square is NGTS-32. The stars are leaving the main sequence and entering the sub-giant branch.

Table 6. Activity indices correlations NGTS-31b and NGTS-32b.

Pearson r		
Index	NGTS-31b	NGTS-32b
BIS	0.02 (0.96)	−0.20 (0.41)
FWHM	−0.27 (0.39)	0.10 (0.66)
S-index	−0.03 (0.92)	0.21 (0.38)
Linear model m		
BIS	-0.01 ± 0.11	$-0.196^{+0.152}_{-0.162}$
FWHM	-0.002 ± 0.045	-0.001 ± 0.045
S-index	-0.0005 ± 0.0447	-0.001 ± 0.0443

as defined by Espinoza, Kossakowski & Brahm (2019), the former of which we fixed to unity during the fitting procedure due to the lack of significant contaminating sources. Since the MEarth light curve shows a clear systematic flux increase with time, a linear trend was included in the model (see Fig. 5). The final parameter related to the light curve is the stellar density, derived from the stellar analysis, which helps decouple the radius ratio and the impact parameter (Sandford et al. 2019; Vines et al. 2019).

The RVs, in turn, are mean subtracted and afterward modelled with a standard Keplerian model, including an instrumental velocity offset γ, a white noise parameter σ, and a first-order acceleration term. In the case of NGTS-32b, we included Gaussian Processes (GP) with a Matern kernel, described by the amplitude a and the characteristic time-scale τ, from `celerite` (Foreman-Mackey et al. 2017) to take into account stellar variability that other methods could not properly model. As a sanity check, we modelled NGTS-32b without GPs, but this model was significantly worse when comparing their BICs.

`EMPEROR.T` utilizes `emcee` v. 2.2.1 and the Parallel Tempering Markov Chain Monte Carlo (PTMCMC) module to perform an initial search of the best-fitting parameters. The following step consists of generating a Gaussian ball around the posterior maximum that works as a starting position for a regular MCMC sampler to gather samples in order to perform parameter inference.

Table 7. Prior choices used in this work.

Parameter	Prior
Orbital parameters	
P [d]	$\ln\mathcal{U}(0.1, 3\max(t_{\rm RV}))$
K [ms^{-1}]	$\mathcal{U}(0, 3\max(\lvert RV\rvert))$
T_c [JD]	$\mathcal{U}(\min(t^a), \max(t))$
ω [rad]	$\pi/2$ (fixed)
e	0 (fixed)
R_p/R_*	$\mathcal{U}(0.01, 0.5)$
b	$\mathcal{U}(0, 1)$
Stellar parameters	
ρ_* [g cm^{-3}]	$\mathcal{N}(d^c, \sigma d^2)$
q_1^b	$\mathcal{U}(0, 1)$
q_2^b	$\mathcal{U}(0, 1)$
RV noise parameters	
γ [ms^{-1}]	$\mathcal{U}(0, 3\max(\lvert RV\rvert))$
σ [ms^{-1}]	$\mathcal{N}(3, 3^2)$
Transit noise parameters	
Offset [ppm]	$\mathcal{N}(0, 0.1^2)$
Jitter [ppm]	$\ln\mathcal{U}(0.1, 10000)$
Dilution	fixed (1)
Acceleration parameters	
$\dot{\gamma}$ [ms^{-1}yr^{-1}]	$\mathcal{U}(-1, 1)$
Trend$_{\rm MEarth}$	$\mathcal{U}(-1, 1)$
GP parameters	
a [m s^{-1}]	$\mathcal{U}(-2, 5)$
τ [log d]	$\mathcal{N}(2.65, 0.25^2)$

[a] t = Time baseline of *TESS* and NGTS data for NGTS-31and NGTS-32, respectively.
[b] Kipping LD parameters.
[c] The prior density is calculated using the radius and mass from Table 5.

The MCMC set-up we used for sampling was: 5 temperatures, 2000 walkers, and 20 000 steps for the PTMCMC, with a burn-in period of half the number of steps, totaling 200 million samples for the search stage, and 2000 walkers with 100 000 steps for the sample gathering stage, which results in 100 million samples used for parameter inference. Each chain of the PTMCMC is affected by a temperature value that effectively flattens the posterior distribution, allowing walkers in higher temperatures to explore the parameter space. The temperatures are provided as $\beta = 1/T$ and each chain has a β parameter of $1/\sqrt{(5)^i}$ with $i = 1, 2, ...T$ and T being the number of temperatures minus one. An aggressive temperature increase makes the walkers' exploration more efficient using fewer chains.

3.2.1 *Prior selection*

We set the period prior as a Jeffreys (log uniform) prior, starting from 0.1 d to three times the total baseline of the RV data. The eccentricity and argument of periastron were fixed to 0 and $\pi/2$, respectively, due to the periods of both planet candidates recovered from the photometry being small (Anderson et al. 2012), and the initial model assessment favoured circular orbits. The other planetary parameters have uniform priors. The instrumental velocity offset has a uniform prior, while the instrumental RV jitter has a zero-mean Gaussian prior. The photometric instrumental priors, however, differ, as the offset has a zero-mean Gaussian prior, and the white noise uses a Jeffreys prior. The dilution was fixed to unity (e.g. no dilution), and the Kipping parameters use a Uniform prior ranging from 0 to 1. The prior details are presented in Table 7.

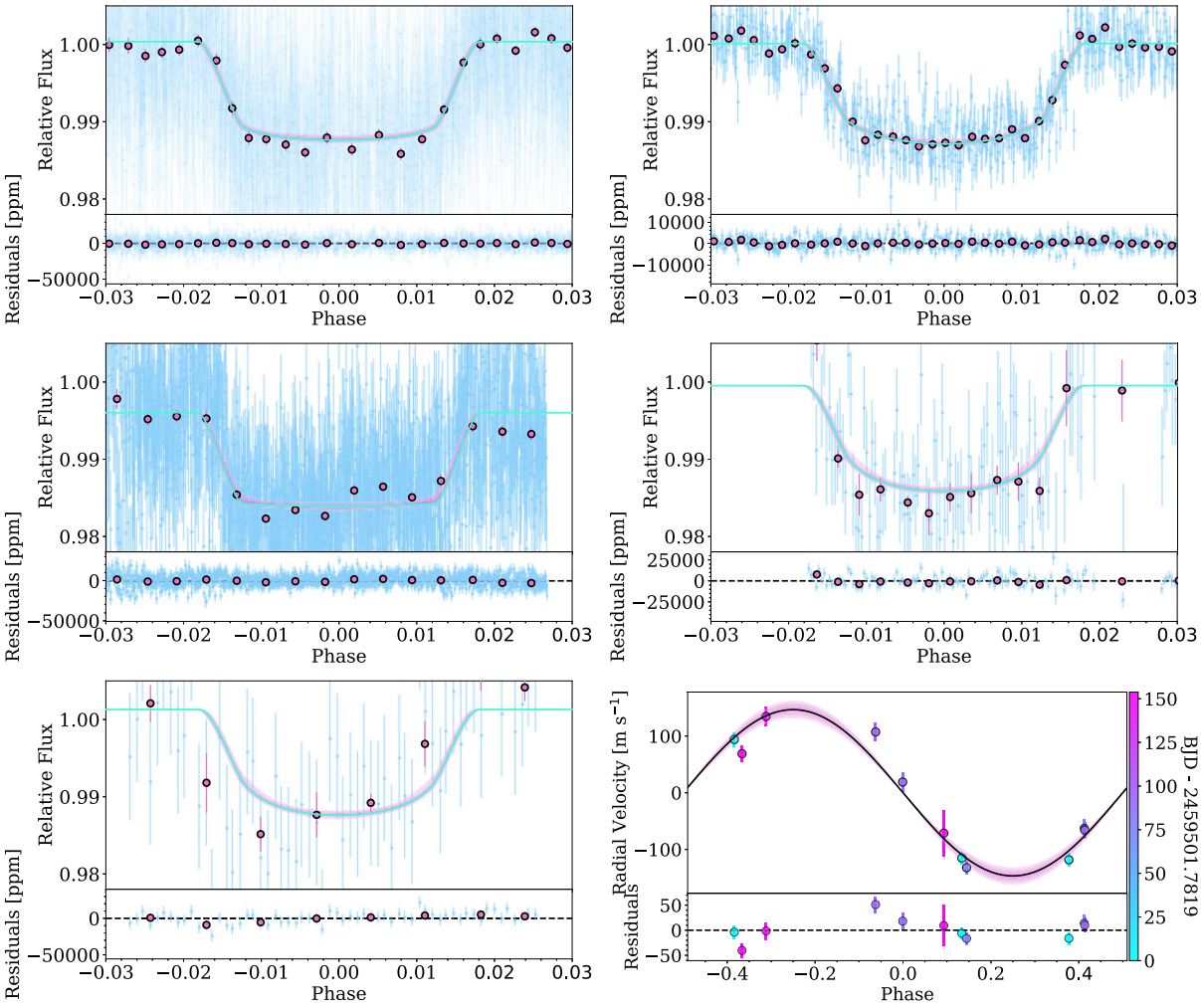

Figure 5. NGTS-31bmodels. Top: The left and right panels are the phase-folded NGTS and TESS light curves, respectively. Middle: This section shows the MEarth and PEST photometric data (left and right, respectively). Bottom: The LCO light curve and the FEROS RVs folded around the best-fitting period. The bands show the 1σ, 2σ, and 3σ confidence intervals for the models. The circles in the photometry panels are the binned photometry in phase space. The bottom panels in each plot show the residuals of the fit.

3.2.2 Model selection

We reran the global modelling using NS through `dynesty` to get the Bayesian evidence (BE) of each model configuration to perform a robust model selection. We used 3000 live points for the NS setup and a stopping criterion of $d \log z < 0.001$, using the same priors defined previously.

3.2.3 NGTS-31

We found that NGTS-31b is a HJ with a period of 4.162734 ± 0.000004 d. We tested two different configurations for the global modelling, one with free eccentricity (with a resulting eccentricity of 0.16 ± 0.01) and another with a circular orbit. The BE difference between the eccentric and ciruclar model is $\Delta\mathcal{Z} = \mathcal{Z}_{\rm ecc} - \mathcal{Z}_{\rm circ} = 4.3$, which is moderate evidence in favour of the eccentric orbit, yet does not reach the threshold of $\Delta\mathcal{Z} \geq 5$. We chose to adopt the circular solution due to this reason and the fact it is a simpler model.

NGTS-31b has a mass and radius of $1.12 \pm 0.12 M_J$ and $1.61 \pm 0.16 R_J$, respectively, resulting in a density of $0.30^{+0.11}_{-0.08}$ g cm^{-3}. We calculated an equilibrium temperature of 1410 ± 20 K (assuming a bond albedo of 0). Fig. 5 shows the phase-folded light curves and RVs for NGTS-31b and the model parameters are summarized in Table 8.

3.2.4 NGTS-32

NGTS-32b is sub-Jovian having a mass, radius, and density of $0.57 \pm 0.05 M_J$, $1.42 \pm 0.03 R_J$, and 0.24 ± 0.03g cm^{-3}, respectively. It has an orbital period of 3.31211 ± 0.00002 d and an equilibrium temperature of 1750 ± 20 K (assuming a bond albedo of 0).

Similarly to NGTS-31b, we tested a model with free eccentricity ($e = 0.081 \pm 0.004$), unlike NGTS-31b, the $\Delta\mathcal{Z}$ for NGTS-32b is just 1.3 in favour of the eccentric orbit, which means that statistically the models are equivalent. Thus, we adopt the circular solution. Due to the significant scatter seen in the RVs, we tested different correlated noise models following the procedure by Vines et al. (2023), with

Table 8. Model parameters for NGTS-31b and NGTS-32b.

Property	Value NGTS-31b	NGTS-32b
Fitted parameters		
P (d)	4.162734 ± 0.000004	3.31211 ± 0.00002
K (m s^{-1})	$146.63^{+8.26}_{-5.97}$	$75.17^{+15.01}_{-0.88}$
e	0 (fixed)	0 (fixed)
w (deg)	90 (fixed)	90 (fixed)
T_C (BJD)	2459039.1615 ± 0.0004	2459435.763 ± 0.002
R_p/R_*	0.110 ± 0.001	0.080 ± 0.001
b	0.63 ± 0.01	0.29 ± 0.01
a/R_*	$8.16^{+0.09}_{-0.08}$	5.28 ± 0.07
Derived parameters		
$M_p(M_J)$	1.12 ± 0.12	0.57 ± 0.05
$R_p(R_J)$	1.61 ± 0.16	1.42 ± 0.03
ρ_p (g cm^{-3})	$0.30^{+0.11}_{-0.08}$	0.24 ± 0.03
Incl (deg)	85.6 ± 0.1	86.9 ± 0.1
a (au)	0.064 ± 0.008	0.044 ± 0.001
T_{eq} (K)	1410 ± 20	1750 ± 20
Other parameters		
$\dot{\gamma}$ (ms^{-1}yr^{-1})	195^{+25}_{-42}	-100^{+73}_{-69}
$\gamma_{\rm FEROS}$ m s^{-1}	-27 ± 8	6^{+11}_{-12}
$\sigma_{\rm FEROS}$ m s^{-1}	6 ± 3	21^{+3}_{-2}
$\gamma_{\rm NGTS}$	-0.00036 ± 0.000042	-0.00046 ± 0.00004
$\sigma_{\rm NGTS}$ (ppm)	6200^{+40}_{-30}	6200^{+40}_{-20}
$\gamma_{\rm TESS}$	-0.00013 ± 0.00003	–
$\sigma_{\rm TESS}$ (ppm)	1110 ± 40	–
$\gamma_{\rm LCO}$	-0.001 ± 0.001	–
$\sigma_{\rm LCO}$ (ppm)	8050^{+1200}_{-230}	–
$\gamma_{\rm MEarth}$	-0.004 ± 0.001	–
$\sigma_{\rm MEarth}$ (ppm)	6000^{+120}_{-210}	–
$\gamma_{\rm PEST}$	-0.0005 ± 0.0005	–
$\sigma_{\rm PEST}$ (ppm)	10^{+50}_{-10}	–
q1$_{\rm NGTS}$	$0.22^{+0.05}_{-0.04}$	0.51 ± 0.05
q2$_{\rm NGTS}$	$0.05^{+0.04}_{-0.03}$	0.84 ± 0.05
q1$_{\rm TESS}$	0.35 ± 0.04	–
q2$_{\rm TESS}$	0.45 ± 0.05	–
q1$_{\rm MEarth}$	$0.00^{+0.028}_{-0.003}$	–
q2$_{\rm MEarth}$	0.60 ± 0.05	–
q1$_{\rm LCO,PEST}$	$0.94^{+0.04}_{-0.05}$	–
q2$_{\rm LCO,PEST}$	0.14 ± 0.05	–
trend$_{\rm MEarth}$	0.029 ± 0.003	–
a (m s^{-1})	–	70.45 ± 0.74
τ (log d)	–	$2.57^{+0.05}_{-0.15}$

the inclusion of Gaussian Processes (GPs) with a Matern kernel. We show a full timeseries model for the RVs in Fig. 14. We show the phase folded NGTS light curve and RVs in Fig. 6 and the model parameters in Table 8.

We note that the GP modelling is essentially recovering the prior, most likely due to the data not being informative enough to constrain the rotation period of the star. Additionally, the fact that the activity analysis did not produce significant correlations between the RVs and the indices, and the high amplitude of the GP suggests there might be stellar activity evolution, possibly spanning years. In fact, other subgiants, such as HD 81 809 A with a reported activity cycle of approximately 8 yr and 40 d (Egeland 2018), or β Hydri with a cycle of 12 yr (Metcalfe et al. 2007). Alternatively, it is possible that additional signals, potentially planetary in nature, remain unresolved in the data set and contribute to the GP's inability to properly sample the stellar rotation period.

4 DISCUSSION

We place these planets in the context of other HJs using the well-studied catalogue from TEPCat[7] (Southworth 2011). We studied the radius-equilibrium temperature diagram (Fig. 7, adapted from Fortney et al. 2021) and, considering the 1σ error on the radii, we find that both planets are significantly above the expected evolution of a pure H/He, 1 M_J.

4.1 Incident flux

From Fig. 8, we can see that NGTS-31b occupies a rather under-populated region in the parameter space, standing above the vast majority of other planets in the same equilibrium temperature bin. Furthermore, the neighbouring planets in the region defined by the 1σ errors in radius and mass around the planet have a mean equilibrium temperature of 1890±200 K, 2.4σ higher than that of NGTS-31b. While NGTS-32b does not stand out amongst other planets with similar equilibrium temperatures, we found that the mean temperature around NGTS-32b is 1520±80, 2.7σ below its own equilibrium temperature.

The general consensus regarding the radius anomaly is that the main parameter driving inflation is the incident flux from the host star. A study from Thorngren & Fortney (2018) found that the conversion of incident flux to interior heating peaks at around 1600 K, and Hartman et al. (2016) find that the radii of HJs correlate with the main-sequence age of their host stars, which become more luminous as they age, providing further evidence that incident flux is one of the main culprits behind inflation. Finally, Demory & Seager (2011) and Miller & Fortney (2011) established a flux threshold of 2×10^5 Wm^{-2} above which inflation occurs.

$$\Delta R = \left(0.70^{+0.07}_{-0.06}\right) \cdot (\log_{10} F - 5.5) \quad (1)$$

$$\Delta R = (0.52 \pm 0.07) \cdot (\log_{10} F - 5.8). \quad (2)$$

We turn to the work by Sestovic et al. (2018; hereafter S18), who developed a hierarchical Bayesian model that relates the expected inflated radius of a planet, to the incident flux it receives. Their work also found a strong correlation between radius inflation and planetary mass, resulting in four distinct models. The two relevant models for this work are equations (1) and (2), where F is the incident flux and ΔR is the expected radius inflation. Equation (1) is valid for masses between $0.37 \leq M < 0.98$ $M_J$and a radius baseline of $0.98 \pm 0.04 R_J$, and equation (2) acts in the mass regime of $0.98 \leq M < 2.5$ M_J and a baseline of $1.06 \pm 0.03 R_J$.

We calculate the incident fluxes of NGTS-31b, and NGTS-32b to be $8.75^{+0.40}_{0.36} \times 10^5$, and $21.15^{+0.98}_{0.97} \times 10^5$ Wm^{-2}, respectively. Using the previous equations, these result in ΔR values of 0.07 ± 0.01 and $0.58 \pm 0.01 R_J$, respectively.

[7] https://www.astro.keele.ac.uk/jkt/tepcat/

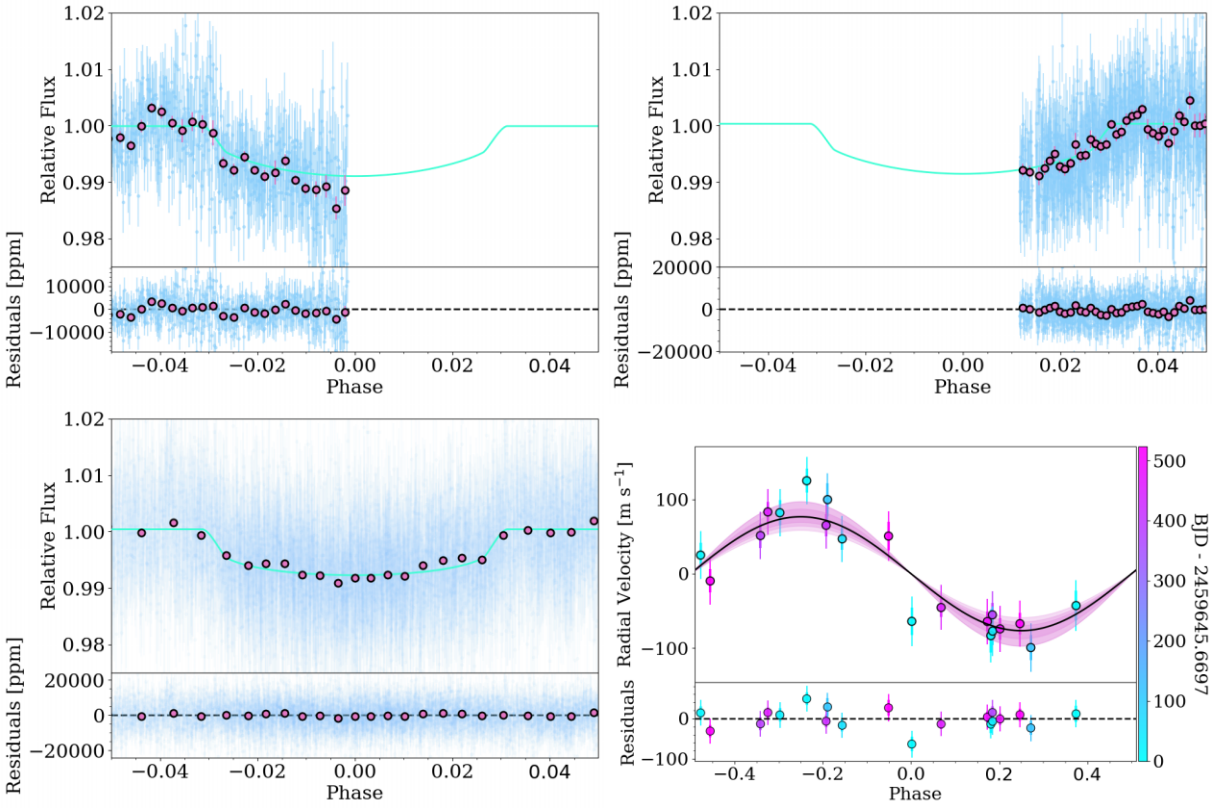

Figure 6. NGTS-32bmodels. Top: Both are the SAAO phase-folded light curves. Bottom: The phase-folded NGTS light curve and the phase-folded FEROS RVs. The bands show the 1σ, 2σ, and 3σ confidence intervals. The circles in the photometry panels are the binned photometry in phase space. The bottom panels show the residuals of the fit.

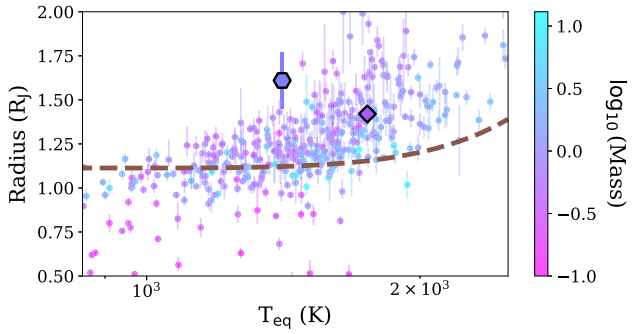

Figure 7. Exoplanets with masses ranging from 0.1 to 13 M_J, where both the masses and radii are determined to better than 20 per cent precision taken from TEPCat (Southworth 2011). Each planet has been colour coded by its mass in $\log_{10}$ scale. The hexagon shows the position of NGTS-31b, while the diamond represents NGTS-32b. The dashed line shows an evolutionary model from Thorngren & Fortney (2018) for a Jovian planet without inflation-inducing effects.

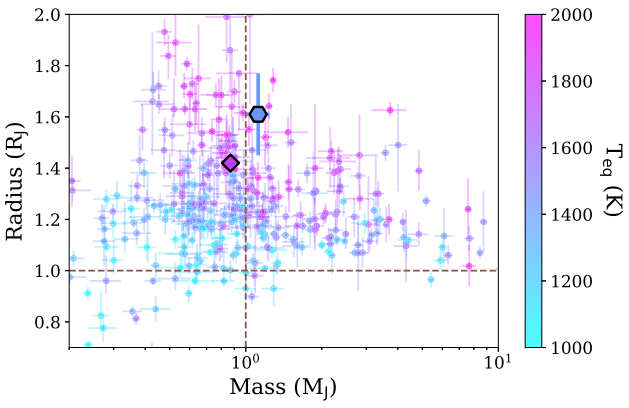

Figure 8. Exoplanets with masses ranging from 0.1 to 13 M_J, (where the masses and radii are determined to better than 20 per cent precision), and equilibrium temperatures between 1000 and 2000 K. Each planet has been colour coded by its equilibrium temperature. The hexagon shows the position of NGTS-31b, while the diamond represents NGTS-32b.

Thus, the expected radius for NGTS-31b reaches $1.13^{+0.14}_{-0.13} R_J$, a significantly lower value than the observed radius of $1.61 \pm 0.16\ R_J$. Conversely, the expected inflated radius of NGTS-32b is calculated to be $1.56 \pm 0.05 R_J$, which is higher than the measured radius ($1.42 \pm 0.03\ R_J$). We contextualize these findings in Fig. 9, where it is conclusively shown that NGTS-31b is excessively inflated, while NGTS-32b is consistent with the expected inflation for its incident flux.

4.2 Other mechanisms

Proposed mechanisms that could drive planetary radii inflation, such as gas giant planets having double-diffusive layered convection instead of fully convective atmospheres (Kurokawa & Inutsuka 2015), or the circularization of HJs formed through high eccentricity formation (Gu, Peng & Yen 2019). Unfortunately, most of these alternative models cannot, by themselves, explain the observed dis-

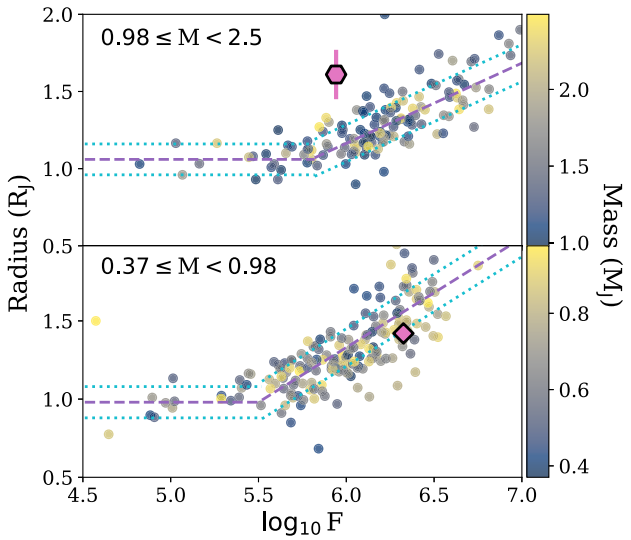

Figure 9. Inflated model according to equation (2) (top) and 1 (bottom). NGTS-31b is shown as a pink hexagon while NGTS-32b is a diamond. It is clear that NGTS-31b is significantly inflated, while NGTS-32b is consistent with the S18 model. The colourbar shows the planetary masses.

tribution of HJs. Of course, there is no reason for a single mechanism to completely drive radius inflation, and indeed, Sarkis et al. (2021) has shown evidence for at least three separate mechanisms acting together.

Another avenue to explain inflated HJs is the possibility of re-inflation post-main-sequence. Komacek et al. (2020) studied the reinflation of warm and hot Jupiters. In particular, they analyzed three reinflated warm Jupiter candidates discovered by Grunblatt et al. (2017, 2019), all with similar radii to NGTS-32b (1.3–1.45 R_J) orbiting evolved stars. From their simulations, Komacek et al. (2020) concluded that with either strong heating and shallow depositing, or inversely, weak heating but deep deposition, they can explain the radii of these planets.

While NGTS-32b is consistent with having an inflated radius considering the scatter in the relation by S18, it is not as inflated as NGTS-31b. Considering both stars are of similar ages (9.97 ± 2.58 Gyr, and $8.03^{+1.03}_{-1.00}$ Gyr for NGTS-31 and NGTS-32, respectively), and that NGTS-32b has a significantly higher incident flux than NGTS-31b. A possible explanation for this is that NGTS-32b is relatively more enriched in metals than NGTS-31b (Fortney, Marley & Barnes 2007).

While both stars are of Solar metallicity, Teske et al. (2019) found that planetary metallicity does not necessarily correlate with the host star metallicity. Furthermore, Thorngren et al. (2016) established a mass–metallicity relation for giant planets where they concluded that giant planets are consistently enriched relative to their host stars. Future atmospheric observations determining the metal enrichment of the planet will provide valuable information, especially considering the planetary radius falls in line with current inflation models.

5 CONCLUSIONS

In this paper, we report the discovery of two hot Jupiter planets: NGTS-31b, NGTS-32b, from NGTS, *TESS*, PEST, LCO, and MEarth photometry and RV data from FEROS, orbiting Solar analogue stars NGTS-31 and NGTS-32. We found the planets to have masses of 1.12 ± 0.12, and 0.57 ± 0.05 M_J respectively, and radii of 1.61 ± 0.16 and $1.42 \pm 0.03 R_J$.

We studied the inflation of each planet and found NGTS-31b to be significantly inflated, especially when compared with other HJs having similar radii and masses. NGTS-32b, on the other hand, is consistent with current radius inflation models. These planets are a valuable addition to the current set of inflated HJs considering their host stars are evolving off the main sequence and their masses fall in the range of $1 \lesssim M_\star \lesssim 1.5$ $M_\odot$, which is the range of stellar masses of stars around which reinflated Jupiters will be most prevalent (Komacek et al. 2020).

Considering the anomalous inflation of NGTS-31b with respect to its equilibrium temperature, and the difference between the expected and observed radius of NGTS-32b, these planets highlight the uncomfortably large scatter in the inflation relations of HJs, and they can serve to test and refine existing models such as S18 or Baraffe et al. (2008).

ACKNOWLEDGEMENTS

Based on data collected under the NGTS project at the ESO La Silla Paranal Observatory. The NGTS facility is operated by the consortium institutes with support from the UK Science and Technology Facilities Council (STFC) projects ST/M001962/1, ST/S002642/1 and ST/W003163/1.

We acknowledge the use of TESS High Level Science Products (HLSP) produced by the Quick-Look Pipeline (QLP) at the TESS Science Office at MIT, which are publicly available from the Mikulski Archive for Space Telescopes (MAST). Funding for the TESS mission is provided by NASA's Science Mission directorate.

This research made use of the PEST photometry pipeline by Thiam-Guan Tan; pestobservatory.com

This work makes use of observations from the LCOGT network.

This research has made use of the Exoplanet Follow-up Observation Program (ExoFOP; DOI: 10.26134/ExoFOP5) website, which is operated by the California Institute of Technology, under contract with the National Aeronautics and Space Administration under the Exoplanet Exploration Program.

JIV acknowledges the support of CONICYT-PFCHA/Doctorado Nacional-21191829. JSJ acknowledges support by Fondecyt grant 1201371 and by the ANID BASAL project FB210003. ML acknowledges support of the Swiss National Science Foundation under grant number PCEFP2_194576. The contributions of FB, ML, and SU have been carried out within the framework of the NCCR PlanetS supported by the Swiss National Science Foundation under grants 51NF40_182901 and 51NF40_205606. The contributions at the Mullard Space Science Laboratory by E.M.B. have been supported by STFC through the consolidated grant ST/W001136/1. SLC acknowledges support from an STFC Ernest Rutherford Fellowship (ST/R003726/1). This project has received funding from the European Research Council (ERC) under the European Union's Horizon 2020 research and innovation programme (grant agreement no 681601). The research leading to these results has received funding from the European Research Council under the European Union's Seventh Framework Programme (FP/2007-2013)/ERC Grant Agreement no. 320964 (WDTracer). KAC acknowledges support from the TESS mission via subaward s3449 from MIT.

DATA AVAILABILITY

The data underlying this article are available in the article and in its online supplementary material.

REFERENCES

Allard F., Homeier D., Freytag B., 2012, Phil. Trans. R. Soc. A: Math. Phys. Eng. Sci., 370, 2765
Alves D. R. et al., 2022, MNRAS, 517, 4447
Anderson D. R. et al., 2011, A&A, 531, A60
Anderson D. R. et al., 2012, MNRAS, 422, 1988
Bailer-Jones C. A. L., Rybizki J., Fouesneau M., Demleitner M., Andrae R., 2021, AJ, 161, 147
Baraffe I., Chabrier G., Barman T., 2008, A&A, 482, 315
Bayliss D. et al., 2018, MNRAS, 475, 4467
Bodenheimer P., Lin D. N. C., Mardling R. A., 2001, ApJ, 548, 466
Boisse I. et al., 2009, A&A, 495, 959
Brahm R., Jordán A., Espinoza N., 2017, PASP, 129, 1
Brasseur C. E., Phillip C., Fleming S. W., Mullally S. E., White R. L., 2019, Astrophysics Source Code Library, record ascl:1905.007
Brown T. M. et al., 2013, PASP, 125, 1031
Burrows A., Hubeny I., Budaj J., Hubbard W. B., 2007, ApJ, 661, 502
Castelli F., Kurucz R. L., 2004, preprint (Astrophysics e-prints), (arXiv:astro-ph/0405087)
Charbonneau D., Brown T. M., Latham D. W., Mayor M., 2000, ApJ, 529, L45
Collier Cameron A. et al., 2006, MNRAS, 373, 799
Collins K. A., Kielkopf J. F., Stassun K. G., Hessman F. V., 2017, AJ, 153, 77
Coppejans R. et al., 2013, PASP, 125, 976
Demory B.-O., Seager S., 2011, ApJS, 197, 12
Díaz R. F., Cincunegui C., Mauas P. J., 2007, MNRAS, 378, 1007
Eaton N., Draper P. W., Allan A., Naylor T., Mukai K., Currie M. J., McCaughrean M., 2014, Astrophysics Source Code Library, record ascl:1405.013
Egeland R., 2018, ApJ, 866, 80
Espinoza N., Kossakowski D., Brahm R., 2019, MNRAS, 490, 2262
Feinstein A. D. et al., 2019, PASP, 131, 094502
Foreman-Mackey D., Agol E., Ambikasaran S., Angus R., 2017, Astrophysics Source Code Library, record ascl:1709.008
Fortney J. J., Marley M. S., Barnes J. W., 2007, ApJ, 659, 1661
Fortney J. J., Dawson R. I., Komacek T. D., 2021, J. Geophys. Res., 126, e06629
Gaia Collaboration, 2023, Astronomy & Astrophysics 674 22
Gomes da Silva J., Santos N. C., Bonfils X., Delfosse X., Forveille T., Udry S., 2011, A&A, 534, A30
Gray D. F., Baliunas S. L., 1995, ApJ, 441, 436
Grunblatt S. K. et al., 2017, AJ, 154, 254
Grunblatt S. K., Huber D., Gaidos E., Hon M., Zinn J. C., Stello D., 2019, AJ, 158, 227
Gu P.-G., Peng D.-K., Yen C.-C., 2019, ApJ, 887, 228
Guillot T., Morel P., Gautier D., Mosser B., Chabrier G., Wuchterl G., 1992, in AAS/Division for Planetary Sciences Meeting Abstracts #24. p. 45.03
Hartman J. D. et al., 2016, AJ, 152, 182
Hauschildt P. H., Allard F., Baron E., 1999, ApJ, 629, 865
Helled R., Lozovsky M., Zucker S., 2016, MNRAS, 455, L96
Henden A., Munari U., 2014, Contrib. Astron. Obs. Skalnate Pleso, 43, 518
Henry G. W., Marcy G. W., Butler R. P., Vogt S. S., 2000, ApJ, 529, L41
Higson E., Handley W., Hobson M., Lasenby A., 2019, Stat. Comput., 29, 891
Hippke M., Heller R., 2019, A&A, 623, A39
Huang C. X. et al., 2020, Res. Notes Am. Astron. Soc., 4, 204
Husser T.-O., von Berg S. W., Dreizler S., Homeier D., Reiners A., Barman T., Hauschildt P. H., 2013, A&A, 553, A6
Irwin J. M., Berta-Thompson Z. K., Charbonneau D., Dittmann J., Falco E. E., Newton E. R., Nutzman P., 2015, preprint (arXiv:1409.0891)
Jeffrey D. S., 1982, ApJ, 263, 835
Jenkins J. S. et al., 2006, MNRAS, 372, 163
Jenkins J. S. et al., 2020, Nat. Astron., 4, 1148
Kaufer A., Stahl O., Tubbesing S., Nørregaard P., Avila G., Francois P., Pasquini L., Pizzella A., 1999, The Messenger, 95, 8
Kipping D. M., 2016, MNRAS, 455, 1680
Komacek T. D., Thorngren D. P., Lopez E. D., Ginzburg S., 2020, ApJ, 893, 36
Kovács G., Zucker S., Mazeh T., 2002, A&A, 391, 369
Kurokawa H., Inutsuka S.-i., 2015, ApJ, 815, 78
Kürster M. et al., 2003, A&A, 403, 1077
Kurucz R., 1993, ATLAS9 Stellar Atmosphere Programs and 2 km/s grid. Kurucz CD-ROM No. 13, Cambridge
Leconte J., Chabrier G., Baraffe I., Levrard B., 2010, A&A, 516, A64
Lomb N. R., 1976, Ap&SS, 39, 447
Lopez E. D., Fortney J. J., 2016, ApJ, 818, 4
Mandel K., Agol E., 2002, ApJ, 580, L171
McCormac J. et al., 2020, MNRAS, 493, 126
McCully C., Volgenau N. H., Harbeck D.-R., Lister T. A., Saunders E. S., Turner M. L., Siiverd R. J., Bowman M., 2018, Proceedings of the SPIE 10707
Metcalfe T. S., Dziembowski W. A., Judge P. G., Snow M., 2007, MNRAS, 379, L16
Miller N., Fortney J. J., 2011, ApJ, 736, L29
Noyes R. W., Hartmann L. W., Baliunas S. L., Duncan D. K., Vaughan A. H., 1984, ApJ, 279, 763
Olmschenk G. et al., 2021, AJ, 161, 273
Parviainen H., 2015, MNRAS, 450, 3233
Pope B. J. S., Parviainen H., Aigrain S., 2016, MNRAS, 461, 3399
Queloz D. et al., 2001, A&A, 379, 279
Queloz D. et al., 2009, A&A, 506, 303
Ricker G. R. et al., 2014, in Oschmann J. M. J., Clampin M., Fazio G. G., MacEwen H. A.eds, Proc. SPIE Conf. Ser. Vol. 9143, Space Telescopes and Instrumentation 2014: Optical, Infrared, and Millimeter Wave. SPIE, Bellingham, p. 914320
Sandford E., Espinoza N., Brahm R., Jordán A., 2019, MNRAS, 489, 3149
Sarkis P., Mordasini C., Henning T., Marleau G. D., Mollière P., 2021, A&A, 645, A79
Schlafly E. F., Finkbeiner D. P., 2011, ApJ, 737 103
Schlegel D. J., Finkbeiner D. P., Marc D., 1998, ApJ, 525, 500
Science Software Branch at STScI, 2012, Astrophysics Source Code Library, record ascl:1207.011
Sestovic M., Demory B.-O., Queloz D., 2018, A&A, 616, A76 (S18)
Skilling J., 2004, in Fischer R., Preuss R., Toussaint U. V.eds, AIP Conf. Ser. Vol. 735, Bayesian Inference and Maximum Entropy Methods in Science and Engineering: 24th International Workshop on Bayesian Inference and Maximum Entropy Methods in Science and Engineering. Am. Inst. Phys., New York, p. 395
Skilling J., 2006, Bayesian Anal., 1, 833
Skrutskie M. F. et al., 2006, AJ, 131, 1163
Sneden C. A., 1973, PhD thesis, The University of Texas at Austin
Soto M. G., Jenkins J. S., 2018, A&A, 615, A76
Soto M. G., Jones M. I., Jenkins J. S., 2021, A&A, 647, A157
Southworth J., 2011, MNRAS, 417, 2166
Speagle J. S., 2020, MNRAS, 493, 3132
Tamuz O., Mazeh T., Zucker S., 2005, MNRAS, 356, 1466
Teske J. K., Thorngren D., Fortney J. J., Hinkel N., Brewer J. M., 2019, AJ, 158, 239
Thorngren D. P., Fortney J. J., 2018, AJ, 155, 214
Thorngren D. P., Fortney J. J., Murray-Clay R. A., Lopez E. D., 2016, ApJ, 831, 64
Tilbrook R. H. et al., 2021, MNRAS, 504, 6018
Toner C. G., Gray D. F., 1988, ApJ, 334, 1008
Vaughan A. H., Preston G. W., Wilson O. C., 1978, PASP, 90, 267
Vines J. I., Jenkins J. S., 2022, MNRAS, 513, 2719–
Vines J. I., et al., MNRAS, 2019, 489, 4125
Vines J. I. et al., 2023, MNRAS, 518, 2627
Weiss L. M. et al., 2013, ApJ, 768, 14
West R. G. et al., 2019, MNRAS, 486, 5094
Wheatley P. J. et al., 2018, MNRAS, 475, 4476
Wright E. L. et al., 2010, AJ, 140, 1868
Wright J. T., Marcy G. W., Howard A. W., Johnson J. A., Morton T. D., Fischer D. A., 2012, ApJ, 753, 160

Zacharias N., Finch C. T., Girard T. M., Henden A., Bartlett J. L., Monet D. G., Zacharias M. I., 2013, AJ, 145, 44
Zechmeister M., Kürster M., 2009, A&A, 496, 577
Zhou G. et al., 2019, AJ, 158, 141
Ziegler C., Tokovinin A., Briceño C., Mang J., Law N., Mann A. W., 2020, AJ, 159, 19
Ziegler C., Tokovinin A., Latiolais M., Briceño C., Law N., Mann A. W., 2021, AJ, 162, 192

SUPPORTING INFORMATION

Supplementary data are available at *MNRAS* online.

suppl_data

Please note: Oxford University Press is not responsible for the content or functionality of any supporting materials supplied by the authors. Any queries (other than missing material) should be directed to the corresponding author for the article.

APPENDIX A: ACTIVITY INDICATOR PLOTS

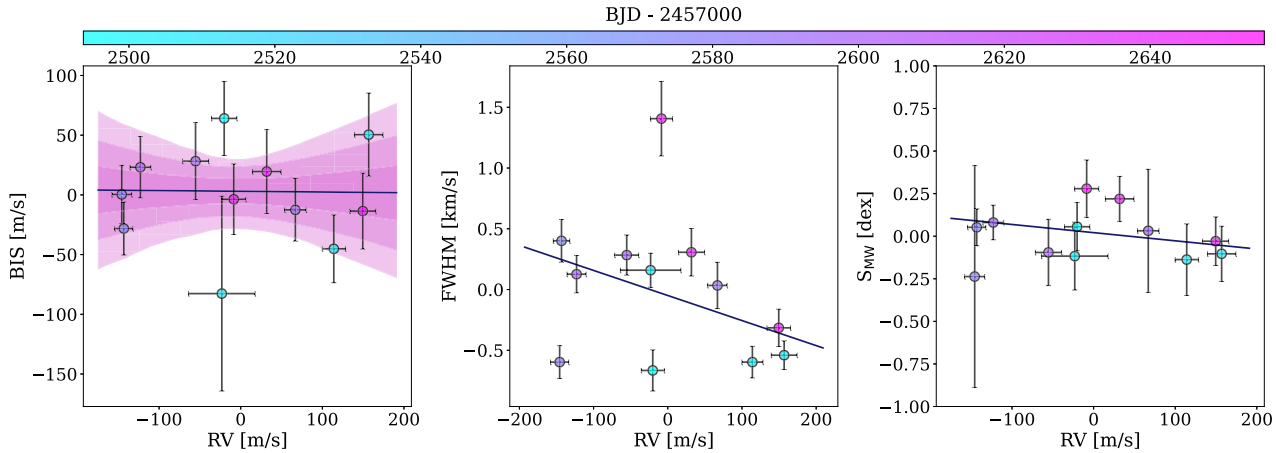

Figure A1. Correlation between the RVs and the BIS (left), FWHM (centre), and S-index (right), colour coded by observation time for NGTS-31b. The bands show the 1σ, 2σ, and 3σ credible intervals, which have been committed in the centre and right panel due to them occupying the whole plot. No significant correlation is found for any of the indicators.

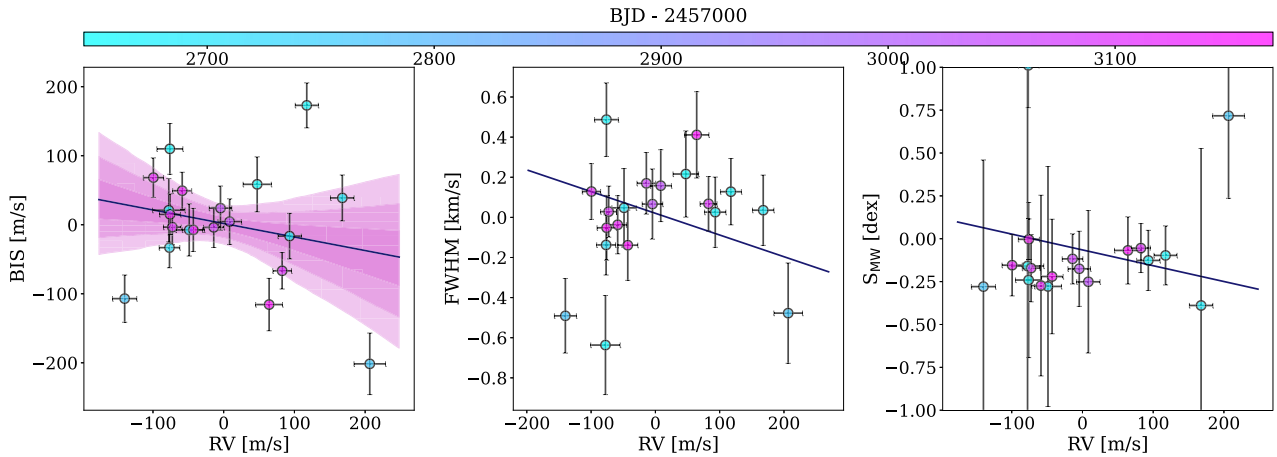

Figure A2. Correlation between the RVs and the BIS (left), FWHM (centre), and S-index (right), colour coded by observation time for NGTS-32b. The bands show the 1σ, 2σ, and 3 σ credible intervals, which have been committed in the centre and right panel due to them occupying the whole plot. No significant correlation is found for any of the indicators.

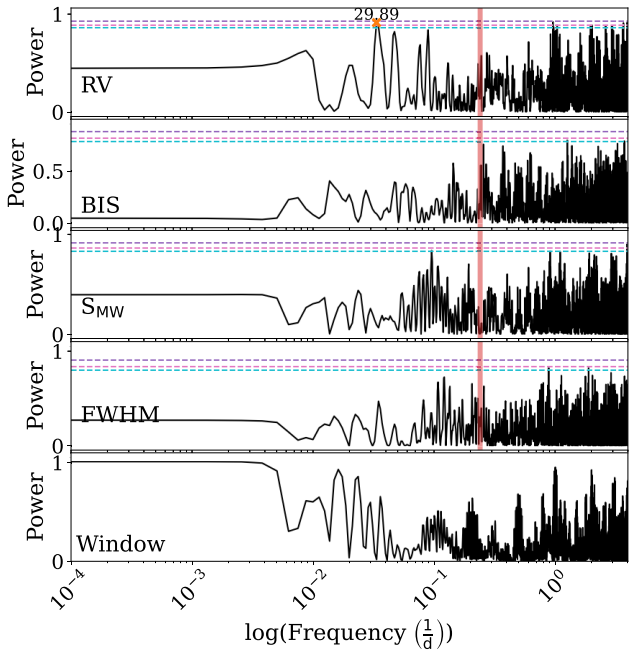

Figure A3. Generalized Lomb Scargle periodogram of the RVs, BIS, S-index and FWHM for NGTS-31b. The vertical line shows the planet period, and the horizontal dashed lines show the 10 per cent (cyan), 1 per cent (pink), and 0.1 per cent (purple) false alarm probability (FAP) lines. There is no significant signal in any of the activity indices.

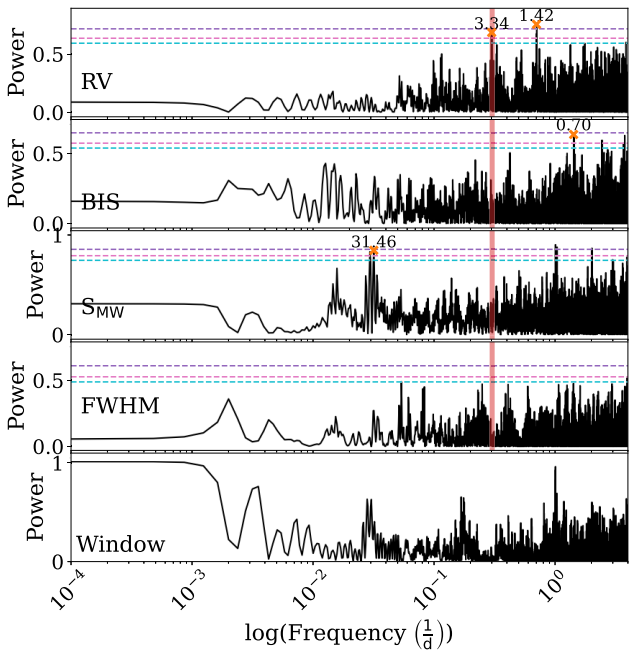

Figure A4. Generalized Lomb-Scargle periodogram of the RVs, BIS, S-index and FWHM for NGTS-32b. The vertical line shows the planet period, and the horizontal dashed lines show the 10 per cent (cyan), 1 per cent (pink), and 0.1 per cent (purple) FAP lines. There is no significant signal in any of the activity indices.

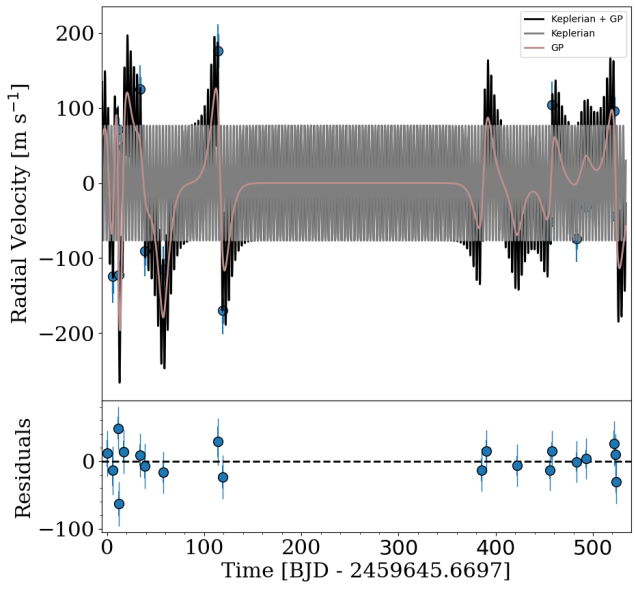

Figure B1. The RV timeseries model for NGTS-32. The black line shows the Keplerian component plus the GP, the grey line shows the Keplerian component alone, while the pink line shows the GP contribution to the model.

APPENDIX B: GAUSSIAN PROCESS IMPACT ON NGTS-32

[1]*Instituto de Astronomía, Universidad Católica del Norte, Angamos 0610, 1270709 Antofagasta, Chile*
[2]*Instituto de Estudios Astrofísicos, Facultad de Ingeniería y Ciencias, Universidad Diego Portales, Av. Ejército 441, 8370191 Santiago, Chile*
[3]*Centro de Astrofísica y Tecnologías Afines (CATA), Casilla 36-D, 7591245, Santiago, Chile*
[4]*Departamento de Astronomía, Universidad de Chile, Camino el Observatorio 1515, 7591245, Casilla 36-D, Santiago, Chile*
[5]*Centre for Exoplanet Research, School of Physics and Astronomy, University of Leicester, University Road, Leicester LE1 7RH, UK*
[6]*Observatoire Astronomique de l'Université de Genève, Chemin Pegasi 51, CH-1290 Versoix, Switzerland*
[7]*Center for Astrophysics | Harvard & Smithsonian, 60 Garden Street, Cambridge, MA 02138, USA*
[8]*Perth Exoplanet Survey Telescope, Perth, Australia*
[9]*Royal Astronomical Society, Burlington House, Piccadilly, London W1J 0BQ, UK*
[10]*Department of Physics and Kavli Institute for Astrophysics and Space Research, Massachusetts Institute of Technology, Cambridge, MA 02139, USA*
[11]*Department of Physics, University of Warwick, Gibbet Hill Road, Coventry CV4 7AL, UK*
[12]*Centre for Exoplanets and Habitability, University of Warwick, Gibbet Hill Road, Coventry CV4 7AL, UK*
[13]*Observatoire Astronomique de l'Université de Genève, Chemin Pegasi 51, CH-1290 Versoix, Switzerland*
[14]*Mullard Space Science Laboratory, University College London, Holmbury St Mary, Dorking RH5 6NT, UK*
[15]*NASA Exoplanet Science Institute, IPAC, MS 100-22, Caltech, 1200 E. California Blvd, Pasadena, CA 91125, USA*
[16]*Institute of Planetary Research, German Aerospace Centre (DLR), Rutherfordstr 2, D-12489 Berlin, Germany*
[17]*Space Telescope Science Institute, 3700 San Martin Drive, Baltimore, MD 21218, USA*

[18]*Astronomy Unit, Queen Mary University of London, Mile End Road, London E1 4NS, UK*
[19]*European Space Agency (ESA), European Space Research and Technology Centre (ESTEC), Keplerlaan 1, NL-2201 AZ Noordwijk, the Netherlands*
[20]*European Southern Observatory, Karl-Schwarzschild-Straße 2, D-85748 Garching bei München, Germany*
[21]*Armagh Observatory & Planetarium, College Hill, Armagh, N Ireland BT61 9DG, UK*
[22]*Department of Aeronautics and Astronautics, MIT, 77 Massachusetts Avenue, Cambridge, MA 02139, USA*
[23]*Department of Astrophysical Sciences, Princeton University, 4 Ivy Lane, Princeton, NJ 08544, USA*

This paper has been typeset from a TEX/LATEX file prepared by the author.